Chemotaxis-Induced Phase Separation

Henrik Weyer,[1,*] David Muramatsu,[1,*] and Erwin Frey[1,2,†]
[1]Arnold Sommerfeld Center for Theoretical Physics and Center for NanoScience, Department of Physics, Ludwig-Maximilians-Universität München, Theresienstraße 37, D-80333 München, Germany
[2]Max Planck School Matter to Life, Hofgartenstraße 8, D-80539 Munich, Germany

(Received 9 September 2024; accepted 22 September 2025; published 10 November 2025)

Chemotaxis allows single cells to self-organize at the population level, as classically described by Keller-Segel models. We show that chemotactic aggregation can be understood using a generalized Maxwell construction based on the balance of density fluxes and reactive turnover. This formulation implies that aggregates generically undergo coarsening, which is interrupted and reversed by cell growth and death. Together, both stable and spatiotemporally dynamic aggregates emerge. Our theory mechanistically links chemotactic self-organization to phase separation and reaction-diffusion patterns.

DOI: 10.1103/2933-45qc

Chemotaxis is a prevalent strategy in biology that enables both microbes and tissue cells to move collectively and directionally in response to chemical gradients [1–5]. This can lead to self-organized aggregation when cells respond to gradients of self-secreted signaling molecules, described by the foundational Keller-Segel (KS) model [6]. Diverse model variants account for different chemotactic responses, crowding effects, and cell proliferation [7]. Without cell proliferation and death, the chemotactic aggregates are observed to undergo a coarsening process [7–12]. In contrast, cell growth and death induce a fixed pattern wavelength, leading to intricate patterning [7,13] and spatiotemporal chaos [14,15], as well as an absorbing-state phase transition with distinct scaling regimes [16]. However, a unifying understanding of chemotactic aggregates and their long-time dynamics in general KS models is missing. It remains unknown whether a generic mechanism links coarsening, the selection of fixed intrinsic wavelengths, and the spatiotemporally dynamic patterns.

In this Letter, we derive the generic behavior of chemotactic aggregates in KS models by developing a combined description of the counteracting effects of random (diffusive) and chemotactic (directed) cell movement. Stationary aggregates are thereby constructed in phase space based on a reactive area balance representing a generalized Maxwell construction. We then argue that the resulting net cell movement drives the coarsening of collections of well-separated aggregates. (Slow) cell growth and death interrupt and reverse the coarsening process, resulting in both fully nonlinear steady-state patterns with fixed wavelengths (aggregate sizes) and spatiotemporally dynamic aggregates. Our theory is independent of the specific mathematical form of the models and relates the macroscopic dynamics of chemotactic aggregates to (active) phase separation [17–19] and (mass-conserving) reaction-diffusion systems [20,21].

We consider a chemotactic population $\rho(\mathbf{x}, t)$ subject to diffusion, with diffusion coefficient D_ρ, and chemotaxis, modeled as advection along the gradients in the chemoattractant field $c(\mathbf{x}, t)$ [6]:

$$\partial_t \rho(\mathbf{x}, t) = D_\rho \nabla^2 \rho - T \nabla[\chi_\rho(\rho)\chi_c(c)\rho \nabla c] + \varepsilon s(\rho). \tag{1}$$

Here, $T\chi_\rho(\rho)\chi_c(c) > 0$ represents the strength of chemotaxis with the positive sensitivity functions χ_ρ and χ_c. For example, χ_ρ may describe crowding effects that suppress chemotaxis, while χ_c may capture nonlinear kinetics of the chemotaxis receptors [7]. Cell growth and death are described by $s(\rho)$ with a dimensionless strength ε. The dynamics of the chemoattractant, produced by the cells and subject to degradation, is given by $\partial_t c(\boldsymbol{x}, t) = D_c \nabla^2 c + f(\rho, c)$. To model net chemoattractant production by the cells, we assume $\partial_\rho f > 0$, biasing f toward chemoattractant production with increasing cell density ρ.

Random cell motion and chemotaxis can be captured in one quantity by rewriting Eq. (1) as

$$\partial_t \rho(\mathbf{x}, t) = T \nabla[\chi_\rho \rho \nabla \eta] + \varepsilon s(\rho), \tag{2}$$

introducing a *mass-redistribution potential* (cf. Refs. [22–24])

*These authors contributed equally to this work.
†Contact author: frey@lmu.de

Published by the American Physical Society under the terms of the Creative Commons Attribution 4.0 International license. Further distribution of this work must maintain attribution to the author(s) and the published article's title, journal citation, and DOI.

$$\eta(\rho(\mathbf{x},t),c(\mathbf{x},t)) \coloneqq \frac{D_\rho}{T}\int_{\rho_0}^{\rho(\mathbf{x},t)} \mathrm{d}\rho \frac{1}{\chi_\rho \rho} - \int_{c_0}^{c(\mathbf{x},t)} \mathrm{d}c \chi_c. \quad (3)$$

Here, we defined two arbitrary reference densities ρ_0 and c_0. The mass-redistribution potential is a function of the local densities ρ and c and, thus, is a spatially varying field. Comparing the sign of the flux term in Eq. (2) with the sign of the chemotaxis term in Eq. (1), it is evident that $\eta(\mathbf{x},t)$ acts as an effective chemorepellent. The effective field η integrates the counteracting effects of diffusion and chemoattraction: It increases with ρ, promoting spreading from high to low densities, and decreases with c, driving aggregation toward regions of high chemoattractant concentration [Eq. (3)].

Mathematically, the mass-redistribution potential η resembles the chemical potential in binary phase separation with the mobility $\chi_\rho \rho$ [cf. Eq. (2) for $\varepsilon = 0$ with model B] [25,26]. However, η is not the derivative of a free energy functional but follows its own dynamic equation; see Ref. [27]. For particular model choices, one can find a relation to a mathematical variational structure [34,35]. The numerical analysis employs the minimal Keller-Segel (mKS) model with $\chi_\rho = \chi_c = 1$ and a linear chemoattractant production and decay term $f = \rho - c$ [36]. Then, one has $\eta = (D_\rho/T)\log\rho - c$. We start our analysis with the mass-conserving dynamics where $\varepsilon = 0$.

Lateral instability—A uniform cell density [homogeneous steady state (hss)] is unstable if chemotactic drift dominates over diffusive spreading, amplifying small density perturbations. From Eq. (2), this requires that η decreases where ρ increases, driving net flux toward denser regions [orange arrows in Figs. 1(a) and 1(b)]. Although η increases with ρ at fixed chemoattractant concentration c (diffusive contribution), cell-density perturbations also alter c through production, potentially causing η to decrease where ρ increases [chemotactic contribution, second term in Eq. (3)]. For long-wavelength modulations, mass redistribution is slow compared to the local relaxation of c, which quickly adjusts to a *quasisteady state* (QSS) $c^*(\rho)$ defined by the nullcline $f(\rho, c^*(\rho)) = 0$. Accordingly, η locally relaxes to the nullcline (NC) $\eta^*(\rho) \coloneqq \eta(\rho, c^*(\rho))$, and chemotactic aggregation becomes self-amplifying if the effective slope is negative:

$$\partial_\rho \eta^*(\rho_{\mathrm{hss}}) < 0. \quad (4)$$

This *nullcline-slope criterion* also holds in the short-wavelength regime (see Appendix A). The instability resembles the mass-redistribution instability found in mass-conserving reaction-diffusion systems as well as spinodal decomposition [21,23].

Stationary aggregate profiles—The stationary, one-dimensional pattern profile $[\tilde{\rho}(x), \tilde{c}(x)]$ can be constructed in the (ρ,η)-phase plane by generalizing local equilibria theory [23,37]. In steady state, the diffusive and chemotactic fluxes must balance; i.e., the total flux $\sim\partial_x\eta$ [cf. Eq. (2)] must vanish throughout domains with no-flux or periodic boundary conditions. Thus, stationary patterns are constrained to the *flux-balance subspace* (FBS) $\tilde{\eta}(x) = \eta_{\mathrm{stat}}$ [Figs. 1(c) and 1(d); η_{stat} is discussed below]. (Well-separated) aggregates are either mesa shaped—with low- and high-density plateaus connected by interfaces [Fig. 1(d)]—or peaks, where density maxima do not saturate in plateaus [Fig. 1(c)]. Plateaus and inflection points, where the curvature $\partial_x^2\tilde{c}$ (approximately) vanishes, are determined by FBS-NC intersections and serve as landmarks of the pattern. In particular, the outer intersections $\rho_\pm$ of a N-shaped NC are approached exponentially by the pattern extrema $\check{\rho}$ and $\hat{\rho}$ as plateau widths increase [sharp-interface approximation in [27]; Fig. 1(d)]. Peak patterns occur if the rightmost FBS-NC intersection ρ_+ does not exist (as in a Λ-shaped NC) or lies at higher densities (asymmetric N-shaped NC) than the total domain mass M set by initial conditions allows for [blue-shaded in Figs. 1(c) and 1(d)]. For example, the mKS model has a Λ-shaped NC allowing unrestricted cell-density growth, while receptor-binding kinetics [38] or volume-filling effects [39,40] lead to N-shaped NCs, directly explaining their density saturation. A mathematical criterion for the transition from peak to mesa patterns is given in Ref. [41].

The reaction NC $\eta^*(\rho)$ separates the (ρ,η) phase plane into regions of net chemoattractant production ($f > 0$) and degradation ($f < 0$). Since η decreases with c at fixed ρ [Eq. (3)], points above the NC correspond to degradation

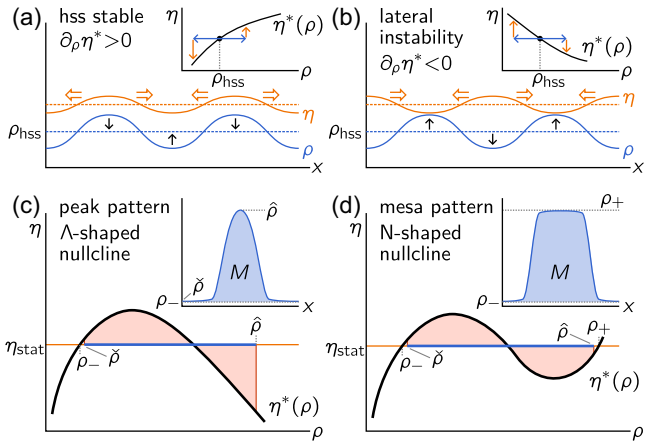


FIG. 1. The mass-redistribution potential (orange) induces redistribution (orange arrows) of the cell density (blue) that counteracts (a) or amplifies (b) initial perturbations (black arrows). (c) Λ-shaped NCs $\eta^*(\rho)$ lead to stationary peak patterns. The low-density intersection between the NC (black) and the flux-balance subspace $\eta = \eta_{\mathrm{stat}}$ (orange) determines the low-density plateau ρ_- (pattern minimum $\check{\rho} \gtrsim \rho_-$). The value η_{stat} is determined by the reactive area balance (balance of the red-shaded areas). (d) N-shaped NCs give an additional high-density NC-FBS intersection ρ_+ (pattern maximum $\hat{\rho} \lesssim \rho_+$). The resulting pattern is mesa shaped.

and points below to production (multistability is discussed in [27]). The FBS position $\eta_{\rm stat}$—previously introduced as an integration constant [42]—sets the vertical placement of the pattern in this phase plane and, thus, the relative contributions of production and degradation. For the pattern to be stationary, $\eta_{\rm stat}$ must self-adjust to balance total production and degradation. This turnover balance is captured by a Maxwell-like area rule between FBS and NC [Figs. 1(c) and 1(d); see Ref. [27]]; for example, in the mKS model: $0 = \int_{\check\rho}^{\hat\rho} \mathrm{d}\rho[\eta_{\rm stat} - \eta^*(\rho)]/\rho$.

Coarsening due to mass competition—In large systems, the KS systems form multiple (quasistationary) aggregates. Intriguingly, a multitude of numerical and mathematical work on specific models showed that these multiple aggregates are not stable but undergo a coarsening process, paralleling Ostwald ripening and coalescence of droplets in phase-separating mixtures [8–12,43–45]. Our framework based on the reactive area balance identifies the model-independent mechanism that explains uninterrupted coarsening in mass-conserving KS systems.

Coarsening proceeds via competition between and coalescence of neighboring aggregates, exemplified for peak patterns in Figs. 2(a) and 2(b). Our analysis (see Appendix B) shows that these processes are caused by *mass competition*: the self-amplifying mass transport along gradients in η, either between aggregates or from one side of the aggregate toward the other. Mass competition arises because the reactive area balance generically implies that $\eta_{\rm stat}$ decreases both with the mass $M = \int \mathrm{d}x(\rho - \rho_-)$ (height) of half-mesas and -peaks (elementary patterns)—at fixed length of the low-density plateau [Fig. 2(a)] and also with decreasing length of the low-density plateau—at fixed mass [Fig. 2(b)]. Within a QSS approximation, η thus decreases during mass competition at the elementary pattern with the already larger peak mass [Fig. 2(a)] or shorter low-density plateau [Fig. 2(b)], resulting in additional mass transport toward these and an amplification of any initial asymmetry. We quantify the growth rates $\sigma_\pm > 0$ of this *mass-competition instability* in the competition and coalescence scenario, respectively, in Appendix B and extend the analysis beyond the QSS approximation in Ref. [46]. This instability makes uninterrupted coarsening a generic feature of mass-conserving Keller-Segel systems and allows its quantification [see Figs. 2(c) and 2(d) and Appendix C]. It unifies previous results for specific systems [8,10,12,44,45,47,48] and likewise accounts for phase-separation-like dynamics in systems where chemotactic drift arises from quorum-sensing-regulated motility [49,50] or from cross-diffusion couplings [24]. Thus, our framework establishes chemotaxis-induced phase separation as part of the broader class of coarsening phenomena in nonequilibrium pattern-forming systems.

Source terms interrupt coarsening—To account for cell growth and death, we now discuss the limit of weakly broken mass conservation ($\varepsilon \ll 1$). Here, the average total density $\bar\rho_{\rm stat}$ of the stationary pattern is determined by the balance of overall production and degradation, $\int_\Omega \mathrm{d}x\, s(\tilde\rho) = 0$ (source balance), not by the initial condition. Thus, a pattern forms only if $0 = s(\rho_{\rm hss})$ holds at a density $\check\rho < \rho_{\rm hss} < \hat\rho$. Otherwise, the system will be homogeneously filled or depleted of cells due to excessive cell growth or death. Moreover, for stability of the elementary (half-mesa or -peak) pattern, the source term s must drive any deviations $\bar\rho - \bar\rho_{\rm stat}$ from the average total density

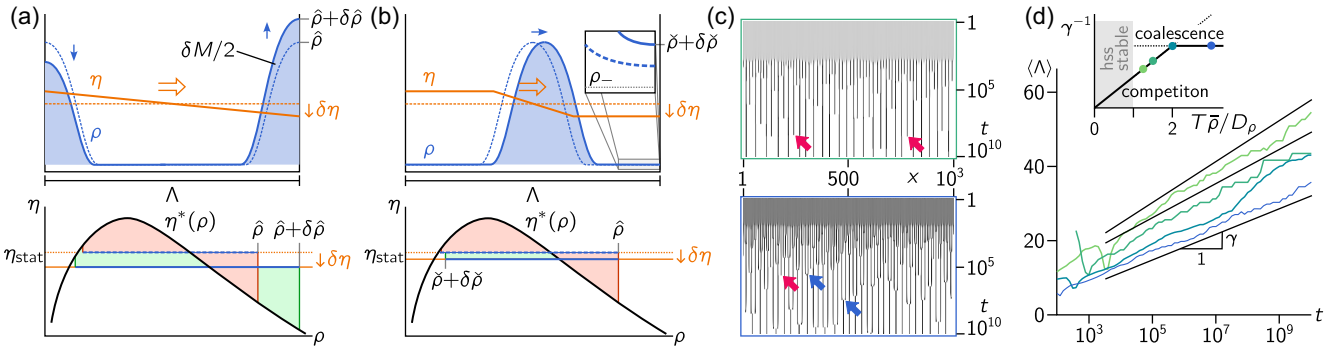


FIG. 2. Illustration of the mass-competition instability for the competition of two peaks (a) and two plateaus [(b); coalescence of the peak with its mirror image] destabilizing the symmetric pattern (dashed lines). In both cases (a) and (b), the changes in the stationary mass-redistribution potentials $\delta\eta$ of the two elementary patterns with the peak mass (blue-shaded areas) and plateau lengths lead to self-amplifying mass transport (orange). The generalized Maxwell area balance (shown for the right elementary patterns in the lower panels) shows that the (quasi)stationary mass-redistribution potential decreases at the larger peak and shorter plateau (red- and green-shaded areas). (c) In a large system, these instabilities induce a coarsening process of the pattern by competition (examples of peak collapse marked by red arrows) and coalescence (blue arrows) as shown in two kymographs of simulations with $T\bar\rho/D_\rho = 1.5, 3$. The faster mass-competition process [cf. inset in (d)] dominates the dynamics. (d) During the coarsening process, the average pattern wavelength $\langle\Lambda\rangle(t)$ continuously grows. Numerical simulations at $T\bar\rho/D_\rho = 1.25, 1.5, 2, 3$ (average over three, one, eight, and two replicates; light green to dark blue) are compared with the prediction $\langle\Lambda\rangle(t) \sim \max(\gamma_\pm)\log(t)$ with $\gamma \propto 5/8, 3/4, 1, 1$ (black lines; see Ref. [27]). Apart from the average density $\bar\rho$ specified above, the simulation parameters are $T = 5$, $D_\rho = 0.1$, and $D_c = 1$, with system length $L = 1000$.

that balances production and degradation back to zero. We, therefore, assume net cell growth at low and net death at high densities as, for example, in logistic growth [cf. Fig. 3(a)]. As mass competition amplifies mass differences, and, hence, differences in $\bar{\rho}$ between elementary patterns, the source term counteracts the mass-competition instability.

To illustrate the counteracting effect, consider the coalescence of a peak with its neighbor (mirror image) [Figs. 2(b) and 3(a)], the dominant coarsening pathway at large $\bar{\rho}_{\mathrm{stat}}$ in the mKS model [Figs. 2(c) and 2(d)]. If the peak shifts right by δx, the right plateau shortens, reducing the total production of cells in the right plateau by approximately $-\varepsilon s(\rho_{-})\delta x$ while production increases by the same amount to the left of the peak, as follows from integration of Eq. (2). As a result, the chemotactic flux of new cells into the aggregate, that balances the degradation of cells inside, is asymmetric and larger on the left side of the aggregate. Thus, the aggregate will shift back toward the symmetric position because more cells accumulate on its left side [Fig. 3(a)]. To this stabilizing, source-induced shift process, the destabilizing mass-competition process due to the η gradients in the first term in Eq. (2) [Fig. 2(b)] must be added. To lowest order in ε, the competition effect can be described using the result for the mass-conserving system (see Appendix D). Mass competition is suppressed if the growth rate of the mass-competition instability under the influence of weak source terms fulfills $\sigma_{\varepsilon}^{-}(\Lambda) \leq 0$. Because the mass-competition rate $\sigma^{-}(\Lambda)$ typically decreases strongly in Λ (exponentially in the mKS model), the mass-competition instability is suppressed above a threshold wavelength Λ_{stop} fulfilling $\sigma_{\varepsilon}^{-}(\Lambda_{\mathrm{stop}}) = 0$ [dotted line in Fig. 3(c)]. Similar formulas follow from the same reasoning for the competition between peaks and for mesa patterns.

Plateau splitting at larger wavelengths—As the source strength or the peak distance is increased further, the source term will increasingly deform the stationary profile compared to the pattern of the mass-conserving system. The weak source terms create weak spatial gradients. These gradients let long plateaus bend inward significantly toward ρ_{hss} [Fig. 3(b); see Ref. [27]]. When the maximum of the low-density plateau (or the minimum of a high-density plateau) enters the region of negative NC slope $\partial_{\rho}\eta^{*} < 0$ at wavelengths $\Lambda \geq \Lambda_{\mathrm{split}}$, the plateau loses stability, and a new peak or mesa is nucleated [Fig. 3(b)] [20,47,51]. Thus, splitting and interrupted coarsening steer the pattern toward a stationary, periodic configuration with a wavelength Λ fulfilling $\Lambda_{\mathrm{stop}} < \Lambda < \Lambda_{\mathrm{split}}$ [Fig. 3(c)].

Successive coalescence and splitting—The scale separation $\Lambda_{\mathrm{stop}} \ll \Lambda_{\mathrm{split}}$ can be lost if the source term (approximately) vanishes at a plateau density $\rho_{\pm}$, as in the mKS model with a logistic growth term $s(\rho) = \rho(p - \rho)$. Far below the splitting threshold Λ_{split}, coalescence is counteracted by production $\varepsilon s(\rho_{-}) \approx \varepsilon\rho_{-}$ in the low-density plateau $\rho_{-} \approx 0$ [Eq. (D1); dotted line in Fig. 3(c)]. In contrast, near the splitting threshold, the plateau deformation inducing splitting is driven by a source term $\sim\varepsilon\rho \gg \varepsilon\rho_{-}$ because the plateau bends upward. Effectively, the source term appears weak for interrupted coarsening but strong for splitting, causing both thresholds to converge already at small source strength ε. Taking into account that the plateau density grows as the splitting threshold Λ_{split} is approached (see Ref. [27]), the threshold of interrupted coarsening Λ_{stop} bends downward [solid blue line in Fig. 3(c)]. Nonetheless, the difference $\Lambda_{\mathrm{split}} - \Lambda_{\mathrm{stop}}$

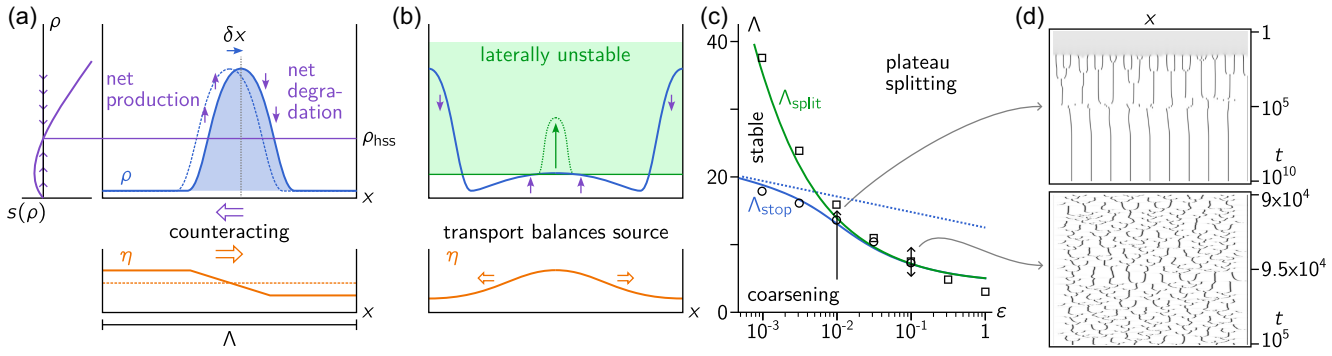


FIG. 3. (a) Illustration of interrupted coarsening due to production and degradation [$s(\rho)$; purple] counteracting the mass-competition instability (orange) which destabilizes the symmetric peak position against shifts δx. (b) Plateau splitting occurs when the plateau density enters the laterally unstable region (green) due to production in the low-density plateau. In mesa patterns, high-density plateaus can split as well due to degradation when the plateau density decreases into the laterally unstable density regime. (c) The stability of patterns with wavelength Λ in the mKS model with a logistic source term $s(\rho) = \rho(1 - \rho)$ of strength ε. The threshold of plateau splitting (green) lies at low wavelengths Λ and deforms the threshold of interrupted coarsening at large source strength ε (solid compared to dashed blue line). The analytic thresholds (lines) well describe the numerical thresholds (circles and squares) obtained by numerical continuation and linear stability analysis (see Ref. [27]). (d) The kymographs show $\log(1 + \rho)$ (grayscale, 0 to 1) for $\varepsilon = 0.01, 0.1$ simulated on a domain with reflective boundaries and length $L = 149, 74$ corresponding (approximately) to a multiple of the mean of the numerical thresholds $\Lambda_{\mathrm{stop,split}}$. The same simulation parameters are used as in Fig. 2(d).

decreases strongly with ε, well describing the numerical results in the mKS model [Fig. 3(c)].

As a result, at moderate source strength ε, several consecutive coalescence and splitting events occur before the stationary, periodic pattern develops [Fig. 3(d), top]. At larger source strength ε, the domain size would have to be fine-tuned for stationary periodic patterns to exist. Instead, the pattern continuously undergoes coalescence and splitting, reaching a dynamic steady state that has been argued to be chaotic [Fig. 3(d), bottom] [14].

Conclusions and outlook—Taken together, we have studied the generic dynamics of chemotactic aggregates using the mass-redistribution potential η, whose gradients fully determine cell migration by integrating random and chemotactic movement. Our geometric construction principle, akin to a Maxwell construction, leverages flux balance and reactive area balance, directly linking to the underlying chemotactic physics.

The construction and macroscopic dynamics closely resemble those in two-component mass-conserving reaction–diffusion systems [20–23,37,52], although pattern formation in KS models is driven by a nonlinear cross-diffusion term, producing a mass-redistribution potential that depends highly nonlinearly on the cell and chemoattractant densities. We expect that the phenomena likewise extend to higher-dimensional systems [10,12,29]. As equilibriumlike pattern constructions were also obtained for scalar active matter [53–60], it is an exciting question how these constructions can be used to classify the coarse-grained dynamics of scalar nonequilibrium matter more generally.

We expect that our theory will offer valuable insights into multispecies chemotactic systems [35,61,62], their interplay with other aggregation mechanisms such as phase separation [63–65], and systems with more complex signaling [66]. In particular, interrupted coarsening and domain splitting may shape the thymus medulla [62]. The predicted phenomena may also be experimentally accessible using engineered bacteria (see, e.g., Ref. [67]). An intriguing open question is whether chemorepelling systems [68] and traveling fronts in systems with chemoattractant consumption or nutrient uptake can be analyzed using a similar framework [69–72]. Finally, understanding how noise affects wavelength selection and spatiotemporally chaotic steady states remains an important challenge for future work.

Acknowledgments—We thank Fridtjof Brauns, Natan Dominko Kobilica, and Florian Raßhofer for inspiring discussions. We thank Alexander Ziepke for his critical reading of the manuscript. This work was funded by the Deutsche Forschungsgemeinschaft (DFG, German Research Foundation) through the Excellence Cluster ORIGINS under Germany's Excellence Strategy—EXC-2094–390783311, the European Union (ERC, CellGeom, Project No. 101097810), and the Chan-Zuckerberg Initiative (CZI). This research was supported in part by Grant No. NSF PHY-2309135 to the Kavli Institute for Theoretical Physics (KITP).

[1] *E. Coli in Motion*, edited by H. C. Berg, *Biological and Medical Physics, Biomedical Engineering* (Springer, New York, NY, 2004).
[2] *Mathematical Biology: II: Spatial Models and Biomedical Applications*, edited by J. D. Murray, Interdisciplinary Applied Mathematics Vol. 18 (Springer, New York, NY, 2003).
[3] C. Gerard and B. J. Rollins, Chemokines and disease, Nat. Rev. Immunol. **2**, 108 (2001).
[4] E. T. Roussos, J. S. Condeelis, and A. Patsialou, Chemotaxis in cancer, Nat. Rev. Cancer **11**, 573 (2011).
[5] X. Trepat, Z. Chen, and K. Jacobson, Cell Migration, in *Comprehensive Physiology*, edited by Y. S. Prakash, 1st ed. (Wiley, New York, 2012), pp. 2369–2392.
[6] E. F. Keller and L. A. Segel, Initiation of slime mold aggregation viewed as an instability, J. Theor. Biol. **26**, 399 (1970).
[7] T. Hillen and K. J. Painter, A user's guide to PDE models for chemotaxis, J. Math. Biol. **58**, 183 (2009).
[8] K. Kang, T. Kolokolnikov, and M. J. Ward, The stability and dynamics of a spike in the 1D Keller–Segel model, IMA J. Appl. Math. **72**, 140 (2007).
[9] E. Kavanagh, Interface motion in the Ostwald ripening and chemotaxis systems, Master's thesis, University of British Columbia, 2014.
[10] M. Meyer, L. Schimansky-Geier, and P. Romanczuk, Active Brownian agents with concentration-dependent chemotactic sensitivity, Phys. Rev. E **89**, 022711 (2014).
[11] L. Rapp and W. Zimmermann, Universal aspects of collective behavior in chemotactic systems, Phys. Rev. E **100**, 032609 (2019).
[12] J. O'Byrne and J. Tailleur, Lamellar to micellar phases and beyond: When tactic active systems admit free energy functionals, Phys. Rev. Lett. **125**, 208003 (2020).
[13] M. Mimura and T. Tsujikawa, Aggregating pattern dynamics in a chemotaxis model including growth, Physica (Amsterdam) **230A**, 499 (1996).
[14] K. J. Painter and T. Hillen, Spatio-temporal chaos in a chemotaxis model, Physica (Amsterdam) **240D**, 363 (2011).
[15] S.-I. Ei, H. Izuhara, and M. Mimura, Spatio-temporal oscillations in the Keller–Segel system with logistic growth, Physica (Amsterdam) **277D**, 1 (2014).
[16] J. van der Kolk, F. Raßhofer, R. Swiderski, A. Haldar, A. Basu, and E. Frey, Anomalous collective dynamics of autochemotactic populations, Phys. Rev. Lett. **131**, 088201 (2023).
[17] S. C. Glotzer, E. A. Di Marzio, and M. Muthukumar, Reaction-controlled morphology of phase-separating mixtures, Phys. Rev. Lett. **74**, 2034 (1995).
[18] D. Zwicker, A. A. Hyman, and F. Jülicher, Suppression of Ostwald ripening in active emulsions, Phys. Rev. E **92**, 012317 (2015).
[19] Y. I. Li and M. E. Cates, Non-equilibrium phase separation with reactions: A canonical model and its behaviour, J. Stat. Mech. (2020) P053206.

[20] F. Brauns, J. Halatek, and E. Frey, Diffusive coupling of two well-mixed compartments elucidates elementary principles of protein-based pattern formation, Phys. Rev. Res. **3**, 013258 (2021).
[21] H. Weyer, F. Brauns, and E. Frey, Coarsening and wavelength selection far from equilibrium: A unifying framework based on singular perturbation theory, Phys. Rev. E **108**, 064202 (2023).
[22] M. Otsuji, S. Ishihara, C. Co, K. Kaibuchi, A. Mochizuki, and S. Kuroda, A mass conserved reaction–diffusion system captures properties of cell polarity, PLoS Comput. Biol. **3**, e108 (2007).
[23] F. Brauns, J. Halatek, and E. Frey, Phase-space geometry of mass-conserving reaction-diffusion dynamics, Phys. Rev. X **10**, 041036 (2020).
[24] M. W. Cotton, R. Golestanian, and J. Agudo-Canalejo, Catalysis-induced phase separation and autoregulation of enzymatic activity, Phys. Rev. Lett. **129**, 158101 (2022).
[25] P. C. Hohenberg and B. I. Halperin, Theory of dynamic critical phenomena, Rev. Mod. Phys. **49**, 435 (1977).
[26] A. J. Bray, Theory of phase-ordering kinetics, Adv. Phys. **51**, 481 (2002).
[27] See Supplemental Material at http://link.aps.org/supplemental/10.1103/2933-45qc for further details and an additional analysis of the model, which includes Refs. [28–33].
[28] L. M. Pismen, *Patterns and Interfaces in Dissipative Dynamics*, Springer Series in Synergetics (Springer-Verlag, Berlin, Heidelberg, 2006).
[29] H. Weyer, T. A. Roth, and E. Frey, Deciphering the interface laws of turing mixtures and foams, arXiv:2409.20070.
[30] M. J. Ward and J. Wei, Asymmetric spike patterns for the one-dimensional Gierer-Meinhardt model-equilibria and stability, Eur. J. Appl. Math. **13**, 283 (2002).
[31] A. Stevens and H. G. Othmer, Aggregation, blowup, and collapse: The ABC's of taxis in reinforced random walks, SIAM J. Appl. Math. **57**, 1044 (1997).
[32] COMSOL Multiphysics, COMSOLAB (2019), https://www.comsol.com/.
[33] P. Virtanen *et al.*, SciPy 1.0: Fundamental algorithms for scientific computing in Python, Nat. Methods **17**, 261 (2020).
[34] D. Horstmann, Lyapunov functions and L^p-estimates for a class of reaction-diffusion systems, Colloquia *Mathematica* **87**, 113 (2001), https://eudml.org/doc/283757.
[35] G. Wolansky, Multi-components chemotactic system in the absence of conflicts, Eur. J. Appl. Math. **13**, 641 (2002).
[36] S. Childress and J. Percus, Nonlinear aspects of chemotaxis, Math. Biosci. **56**, 217 (1981).
[37] J. Halatek and E. Frey, Rethinking pattern formation in reaction–diffusion systems, Nat. Phys. **14**, 507 (2018).
[38] L. A. Segel, A theoretical study of receptor mechanisms in bacterial chemotaxis, SIAM J. Appl. Math. **32**, 653 (1977).
[39] T. Hillen and K. Painter, Global existence for a parabolic chemotaxis model with prevention of overcrowding, Adv. Appl. Math. **26**, 280 (2001).
[40] K. Painter and T. Hillen, Volume-filling and quorum-sensing in models for chemosensitive movement, Can. Appl. Math. Q. **10**, 501 (2002).
[41] T. Hillen, A classification of spikes and plateaus, SIAM Rev. **49**, 35 (2007).
[42] R. Schaaf, Stationary solutions of chemotaxis systems, Trans. Am. Math. Soc. **292**, 531 (1985).
[43] A. Dinelli, J. O'Byrne, and J. Tailleur, Fluctuating hydrodynamics of active particles interacting via taxis and quorum sensing: Static and dynamics, J. Phys. A **57**, 395002 (2024).
[44] Y. Dolak and C. Schmeiser, The Keller–Segel model with logistic sensitivity function and small diffusivity, SIAM J. Appl. Math. **66**, 286 (2005).
[45] A. B. Potapov and T. Hillen, Metastability in chemotaxis models, J. Dyn. Differ. Equ. **17**, 293 (2005).
[46] H. Weyer, D. Muramatsu, and E. Frey, companion paper, Coarsening dynamics of chemotactic aggregates, Phys. Rev. E **112**, 054406 (2025).
[47] T. Kolokolnikov, J. Wei, and A. Alcolado, Basic mechanisms driving complex spike dynamics in a chemotaxis model with logistic growth, SIAM J. Appl. Math. **74**, 1375 (2014).
[48] F. Kong, M. J. Ward, and J. Wei, Existence, Stability and slow dynamics of spikes in a 1D minimal Keller–Segel model with logistic growth, J. Nonlinear Sci. **34**, 51 (2024).
[49] X. Fu, L.-H. Tang, C. Liu, J.-D. Huang, T. Hwa, and P. Lenz, Stripe formation in bacterial systems with density-suppressed motility, Phys. Rev. Lett. **108**, 198102 (2012).
[50] J. Tailleur and M. E. Cates, Statistical mechanics of interacting run-and-tumble bacteria, Phys. Rev. Lett. **100**, 218103 (2008).
[51] T. Kolokolnikov, M. Ward, and J. Wei, Self-replication of mesa patterns in reaction–diffusion systems, Physica (Amsterdam) **236D**, 104 (2007).
[52] S. Ishihara, M. Otsuji, and A. Mochizuki, Transient and steady state of mass-conserved reaction-diffusion systems, Phys. Rev. E **75**, 015203 (2007).
[53] A. P. Solon, J. Stenhammar, M. E. Cates, Y. Kafri, and J. Tailleur, Generalized thermodynamics of motility-induced phase separation: Phase equilibria, Laplace pressure, and change of ensembles, New J. Phys. **20**, 075001 (2018).
[54] A. P. Solon, J. Stenhammar, M. E. Cates, Y. Kafri, and J. Tailleur, Generalized thermodynamics of phase equilibria in scalar active matter, Phys. Rev. E **97**, 020602 (2018).
[55] E. Tjhung, C. Nardini, and M. E. Cates, Cluster phases and bubbly phase separation in active fluids: Reversal of the Ostwald process, Phys. Rev. X **8**, 031080 (2018).
[56] G. Fausti, E. Tjhung, M. E. Cates, and C. Nardini, Capillary interfacial tension in active phase separation, Phys. Rev. Lett. **127**, 068001 (2021).
[57] A. K. Omar, H. Row, S. A. Mallory, and J. F. Brady, Mechanical theory of nonequilibrium coexistence and motility-induced phase separation, Proc. Natl. Acad. Sci. U.S.A. **120**, e2219900120 (2023).
[58] L. Langford and A. K. Omar, Theory of capillary tension and interfacial dynamics of motility-induced phases, Phys. Rev. E **110**, 054604 (2024).
[59] M. E. Cates and C. Nardini, Classical nucleation theory for active fluid phase separation, Phys. Rev. Lett. **130**, 098203 (2023).
[60] L. Langford and A. K. Omar, The mechanics of nucleation and growth and the surface tensions of active matter, arXiv:2407.06462.

[61] W. Liu, J. Cremer, D. Li, T. Hwa, and C. Liu, An evolutionarily stable strategy to colonize spatially extended habitats, Nature (London) **575**, 664 (2019).
[62] D. Muramatsu, H. Weyer, F. M. Gartner, and E. Frey, Basic interactions responsible for thymus function explain the convoluted medulla shape, Proc. Natl. Acad. Sci. U.S.A. **122**, e2415288122 (2025).
[63] H. Zhao, A. Košmrlj, and S. S. Datta, Chemotactic motility-induced phase separation, Phys. Rev. Lett. **131**, 118301 (2023).
[64] L. Demarchi, A. Goychuk, I. Maryshev, and E. Frey, Enzyme-Enriched condensates show self-propulsion, positioning, and coexistence, Phys. Rev. Lett. **130**, 128401 (2023).
[65] A. Goychuk, L. Demarchi, I. Maryshev, and E. Frey, Self-consistent sharp interface theory of active condensate dynamics, Phys. Rev. Res. **6**, 033082 (2024).
[66] A. Ziepke, I. Maryshev, I. S. Aranson, and E. Frey, Multi-scale organization in communicating active matter, Nat. Commun. **13**, 6727 (2022).
[67] A. I. Curatolo, N. Zhou, Y. Zhao, C. Liu, A. Daerr, J. Tailleur, and J. Huang, Cooperative pattern formation in multi-component bacterial systems through reciprocal motility regulation, Nat. Phys. **16**, 1152 (2020).
[68] B. Liebchen, D. Marenduzzo, I. Pagonabarraga, and M. E. Cates, Clustering and pattern formation in chemorepulsive active colloids, Phys. Rev. Lett. **115**, 258301 (2015).
[69] M. J. Tindall, P. K. Maini, S. L. Porter, and J. P. Armitage, Overview of mathematical approaches used to model bacterial chemotaxis II: Bacterial populations, Bull. Math. Biol. **70**, 1570 (2008).
[70] J. Adler, Chemotaxis in bacteria: Motile Escherichiacoli migrate in bands that are influenced by oxygen and organic nutrients, Science **153**, 708 (1966).
[71] E. O. Budrene and H. C. Berg, Dynamics of formation of symmetrical patterns by chemotactic bacteria, Nature (London) **376**, 49 (1995).
[72] J. Cremer, T. Honda, Y. Tang, J. Wong-Ng, M. Vergassola, and T. Hwa, Chemotaxis as a navigation strategy to boost range expansion, Nature (London) **575**, 658 (2019).
[73] J. Langer, Theory of spinodal decomposition in alloys, Ann. Phys. (N.Y.) **65**, 53 (1971).
[74] K. B. Glasner and T. P. Witelski, Coarsening dynamics of dewetting films, Phys. Rev. E **67**, 016302 (2003).
[75] T. Kolokolnikov, T. Erneux, and J. Wei, Mesa-type patterns in the one-dimensional Brusselator and their stability, Physica (Amsterdam) **214D**, 63 (2006).

End Matter

Appendix A: Nullcline-slope criterion exact for short-wavelength perturbations—The nullcline-slope criterion predicts the stability of the hss against chemotactic aggregation. It is derived above using a QSS approximation in the long-wavelength limit. For short-wavelength perturbations resulting in fast mass redistribution, the QSS approximation does not include the timescale of the local reactive relaxation of η onto $\eta^*(\rho)$. Nevertheless, $\eta^*(\rho)$ still sets the relaxation direction, and the nullcline-slope criterion [Eq. (4)] remains valid: It determines whether η increases or decreases in regions of increased cell density ρ and, thus, whether uniform densities are destabilized [46].

Appendix B: Quantifying coarsening of chemotactic aggregates—To understand the dynamics of patterns with several domains (peaks or mesas), we describe the interaction between two elementary pattern motifs (two half-peak or two half-mesa patterns). As illustrated for peaks in the following, the pattern domains can interact either via competition for mass or coalescence with neighbors (mirror image) [Figs. 2(a) and 2(b); reflective boundaries]. Assuming a slow evolution of the pattern after each *single* elementary pattern relaxed to its (quasi)stationary profile, we approximate the mass-redistribution potential at the single interfaces by its stationary value η_{stat} (QSS approximation). Via the reactive area balance, η_{stat} depends on the extremal densities $\check{\rho}$ and $\hat{\rho}$ of the elementary pattern [Figs. 2(a) and 2(b)]. Consequently, differences in peak height or in the width of the upper and lower plateau regions generate η gradients: Changes in the plateau lengths shift $\check{\rho}$ or $\hat{\rho}$ exponentially, thereby altering η_{stat}. For peak patterns, where the upper plateau is absent, the peak mass directly sets the height $\hat{\rho}$ and, thus, determines η_{stat}. All such changes of the pattern reflect effective changes of the mass M of the elementary pattern, since changes in plateau length due to a shift of the peak or mesa interface [cf. Fig. 2(b)] require mass changes $\delta M \approx \pm(\hat{\rho}-\check{\rho})\delta l$; the sign distinguishes whether the upper or lower plateau is varied. The corresponding partial derivatives of the stationary mass-redistribution potential are denoted by $\partial_M^{\pm}\eta_{\mathrm{stat}}$. Since the geometry of the reactive area balance is model independent, it generically implies $\partial_{\hat{\rho},\check{\rho}}\eta_{\mathrm{stat}} \lesseqgtr 0$ and, with the above definition of δM, $\partial_M^{\pm}\eta_{\mathrm{stat}} < 0$ for both peak and mesa patterns, assuming that $\hat{\rho}$ increases with mass in peaks [Figs. 2(a) and 2(b)].

In peak competition [Fig. 2(a)], the mass difference δM of the two peaks generates an η gradient $\sim\partial_M^{+}\eta_{\mathrm{stat}}/\Lambda$ that drives mass redistribution; the larger peak grows, the smaller collapses. In coalescence [Fig. 2(b)], unequal plateau widths shift η_{stat}, inducing a gradient $\sim\partial_M^{-}\eta_{\mathrm{stat}}/\ell_{\mathrm{int}}$ within the peak of half-width ℓ_{int}. This gradient drives peak motion until the shorter plateau vanishes. In both cases, the symmetric configuration is destabilized by a mass-competition instability. Its growth rates $\sigma_{\pm}$ are derived in Supplemental Material [27] within the QSS approximation and in Ref. [46] using singular perturbation theory. Singular perturbation theory shows that the instability (coarsening) criteria $\partial_M^{\pm}\eta_{\mathrm{stat}} < 0$ remain exact beyond the QSS approximation.

In terms of diffusion and chemotaxis, what causes generic aggregate coarsening analogously to Ostwald ripening? Linear stability of the low-density plateau requires $\partial_\rho \eta^*|_{\rho_-} > 0$ and $\partial_c f(\rho_-, c_-) < 0$, which together imply $\partial_\rho c^*|_{\rho_-} = -\partial_\rho f/\partial_c f|_{\rho_-} > 0$. Accordingly, $\partial_M^+ \eta_{\mathrm{stat}} < 0$ implies $\partial_M^+ \rho_- < 0$, such that cells diffuse toward larger aggregates because these deplete the surrounding low-density plateau more strongly. In contrast, chemotaxis drives cells toward smaller aggregates since $\partial_M^+ c_- < 0$, but the generic finding $\partial_M^\pm \eta_{\mathrm{stat}} < 0$ implies that the diffusive flux dominates. Taken together, although chemotaxis biases motion of cells toward smaller aggregates, their random motion dominates in the surrounding low-density plateaus and leads to the growth of larger aggregates. These deplete their surroundings more strongly, resulting in aggregate coarsening.

Appendix C: Coarsening in the mKS model—In the mKS model, we find $\sigma^\pm \sim \exp(-\Lambda/\gamma_\pm)$, where Λ is the wavelength of the pattern [Figs. 2(a) and 2(b)] and $\gamma_\pm$ are length scales related to the exponential approach of the pattern profile toward $\rho_\pm$ (see Refs. [27,46]). One has $\gamma_- \gtrless \gamma_+$ for $\bar{\rho} \gtrless 2D_\rho/T$ [Fig. 2(d), inset]. Consequently, coalescence is faster for large average densities $\bar{\rho} > 2D_\rho/T$ (competition at low densities $\bar{\rho} < 2D_\rho/T$) and dominates the coarsening process at large wavelengths. This prediction agrees with the observations in numerical kymographs [Fig. 2(c)]. As $[\sigma^\pm(\langle\Lambda\rangle)]^{-1}$ is the typical timescale on which peaks vanish via competition or coalescence at the mean pattern wavelength $\langle\Lambda\rangle$ (and strongly increases with $\langle\Lambda\rangle$), the time during coarsening scales as $t^{-1} \sim \sigma^\pm(\langle\Lambda\rangle)$ [21,73,74]; see Ref. [27]. The resulting coarsening law $\langle\Lambda\rangle \sim \max(\gamma_\pm) \log t$ describes numerical simulations well, with deviations at the transition from competition- to coalescence-dominated coarsening [Fig. 2(d)].

Appendix D: Mass competition under the influence of weak source terms—The effect of the source term onto the coalescence of neighboring peaks [Fig. 3(a)] can be analyzed by making a traveling-wave ansatz $\rho(x,t) = \tilde{\rho}[x - \delta x(t)]$ for the aggregate. Integrating Eq. (2) from the peak maximum to the right boundary, one finds $(\hat{\rho} - \rho_-)\partial_t^{\mathrm{source}} \delta x \approx -\varepsilon s(\rho_-)\delta x$, which drives the peak back to its symmetric position $\delta x = 0$ (see Ref. [27]). Moreover, to lowest order in ε, the destabilizing mass-competition effect due to η gradients within the peak is described by the result $\partial_t^{\mathrm{comp}} \delta x \approx \sigma_{\mathrm{D}}^- \delta x$ for the mass-conserving system. Together, one obtains the growth rate of the mass-competition instability under the influence of weak source terms (for $\varepsilon \ll 1$; cf. Refs. [8,47,48] and [20,21,75] for the analogous effect in two-component reaction-diffusion systems)

$$\sigma_\varepsilon^-(\Lambda) \approx \sigma_{\mathrm{D}}^-(\Lambda) - \varepsilon \frac{s(\rho_-)}{\hat{\rho}(\Lambda) - \rho_-}. \tag{D1}$$

Here, $\sigma_{\mathrm{D}}^-(\Lambda)$ denotes the diffusion-limited part of the growth rate σ^-. A detailed derivation is given in Supplemental Material [27].